One-step parity measurement of *N* cat-state qubits via reverse engineering and optimal control

Dong-Sheng Li,[1,2] Yi-Hao Kang,[1,2,3,*] Ye-Hong Chen,[1,2,4,†] Yang Liu,[1,2]
Cheng Zhang,[1,2] Yu Wang,[5] Jie Song,[3] and Yan Xia[1,2,‡]

[1]*Fujian Key Laboratory of Quantum Information and Quantum Optics, Fuzhou University, Fuzhou 350108, China*
[2]*Department of Physics, Fuzhou University, Fuzhou 350108, China*
[3]*Department of Physics, Harbin Institute of Technology, Harbin 150001, China*
[4]*Theoretical Quantum Physics Laboratory, Cluster for Pioneering Research, RIKEN, Wako-shi, Saitama 351-0198, Japan*
[5]*School of Physics, Hangzhou Normal University, Hangzhou 311121, China*

(Received 11 October 2023; accepted 1 February 2024; published 26 February 2024)

In this paper, a one-step protocol is proposed for the parity measurement of *N* cat-state qubits which are encoded on the cat states of the modes in superconducting Kerr-nonlinear cavities. The parity measurement is performed with the help of an auxiliary qutrit. Especially, the auxiliary qutrit can (cannot) be excited to the higher-energy levels when the cat-state qubits are in the even- (odd-) parity state. By designing the Rabi frequency of the classical fields via reverse engineering and optimal control, the qutrit is driven to an excited dressed state in the even-parity case, which is robust to the systematic errors of the qutrit-cavity coupling strengths. Accordingly, the parity of the cat-state qubits can be distinguished with high accuracy by measuring the final population of the ground state of the auxiliary qutrit. Numerical simulations also show that the protocol is insensitive to the systematic errors of the classical fields, the inhomogeneity of the coupling strengths, intercavity cross talk, unwanted qutrit transitions, and decoherence. Therefore, the protocol may provide an effective approach for parity measurement of multiple cat-state qubits.

DOI: 10.1103/PhysRevA.109.022437

I. INTRODUCTION

Parity measurement [1–6], as a powerful tool to analyze the symmetry of quantum states, is significant for quantum information processing. For example, parity measurement has various applications in entanglement distillation and purification [7–11], entanglement swapping [12–14], entanglement fusing [15–17], quantum teleportation [18–20], and quantum-phase-transition observation [21]. As a result of the above applications, parity measurement has been studied in different physical qubits, such as photons [22–24], superconducting qubits [25–28], neutral atoms [29–31], trapped ions [32], and spins [33,34]. These studies [22–34] greatly benefit parity-measurement-based quantum information tasks with physical qubits.

Recently, increasing research interest has focused on quantum information processing with logical qubits [35–39]. Compared with a physical qubit, a logical qubit possesses some additional degrees of freedom and is useful in quantum error correction [40–43], improving the performance of quantum information tasks. Typically, two ways to construct a logical qubit exist: One is integrating many physical qubits together [44–47]; the other is using bosonic modes [48–52]. Logical qubits constructed via the latter are referred to as bosonic qubits [53,54]. Since bosonic qubits allow quantum error correction to extend the number of excitation qubits instead of the number of physical qubits, the noise channels remain unchanged [55–57]. Accordingly, the physical resources for quantum error correction can be reduced.

The cat-state qubit, encoding quantum information on a pair of cat states, is a promising type of bosonic qubit in the field of quantum information processing with a lot of advantages [58–62]. First, cat-state qubits are noise biased; i.e., they mainly experience bit-flip noise, while the phase-flip errors are exponentially suppressed [59,63]. Additional layers of error correction can focus only on the bit-flip error, so the number of building blocks is significantly reduced. Moreover, a cat-state qubit has an enhanced lifetime with quantum error correction [64]. Because of the advantages of cat-state qubits, many protocols [65–70] have been proposed for quantum computation with cat-state qubits. However, parity measurement of multiple cat-state qubits is rarely studied, although parity measurement is an important means to realize quantum computation and quantum information processing. Therefore, in order to further construct a complete quantum toolbox for large-scale quantum information processing based on cat-state qubits, it is also necessary to extend the parity measurement to the system composed of multiple cat-state qubits.

In this paper, a protocol is proposed for implementing parity measurement of *N* cat-state qubits in one step. The physical model comprises *N* Kerr-nonlinear cavities and an auxiliary qutrit. The evolution of each cavity is confined to a cat-state subspace by utilizing strong Kerr nonlinearity,

*1417378474@qq.com
†yehong.chen@fzu.edu.cn
‡xia-208@163.com

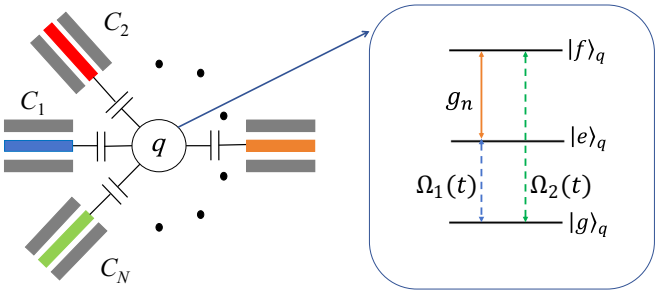

FIG. 1. The physical model of N superconducting Kerr-nonlinear resonators (cavities) coupling to an auxiliary qutrit.

forming a cat-state qubit [71,72]. The qutrit is resonantly coupled to all Kerr-nonlinear cavities and is driven by a pair of classical fields. By properly modulating the frequencies of the classical fields, we derive an effective Hamiltonian for the parity-selective qutrit transition. When the cat-state qubits are in the even-parity states, the qutrit can be excited to a dressed state of two higher-energy levels after certain operations. However, the qutrit remains in the ground level when the cat-state qubits are in the odd-parity states. Consequently, the parity of the cat-state qubits can be distinguished by measuring the final population of the ground level of the auxiliary qutrit.

To reduce the influence of the systematic errors of the coupling strengths, we design time-dependent control fields using reverse engineering [73,74] and optimal control [75,76]. With the help of the designed control fields, the parity measurement is implemented with robustness against systematic errors of the coupling strengths. We also numerically estimate the performance of the protocol in the presence of several disturbing factors. The results demonstrate that the protocol is also insensitive to systematic errors of the classical fields, the inhomogeneity of the coupling strengths, the intercavity cross talk, unwanted transitions, and decoherence. Therefore, the protocol may be promising for parity measurement of multiple cat-state qubits.

This paper is organized as follows. In Sec. II, we describe the physical model for the parity measurement of N cat-state qubits with an auxiliary qutrit and give the concrete form of the Hamiltonian. In order to realize the parity-selective qutrit transition, we derive an effective Hamiltonian by setting proper parameters. In Sec. III, we use reverse engineering and optimal control to determine the evolution path and suppress the influence of the systematic errors in the coupling strengths, respectively. In Sec. IV, using numerical simulations, we confirm the feasibility of the protocol and estimate the performance of the protocol in the presence of systematic errors, the inhomogeneity of the coupling strengths, the intercavity cross talk, unwanted transitions, and decoherence. Finally, conclusions are given in Sec. V.

II. PHYSICAL MODEL

In this section, we introduce the physical model for implementing the parity measurement of N cat-state qubits. As shown in Fig. 1, the physical system contains N Kerr-nonlinear cavities and an auxiliary qutrit. A resonant single-mode two-photon (i.e., quadrature) squeezing drive with strength ϵ_n is applied to the nth Kerr-nonlinear cavity mode C_n ($n = 1, 2, \ldots, N$). The Hamiltonian [71,72] for the cavities is written as ($\hbar = 1$)

$$H_0 = \sum_{n=1}^{N} -K_n a_n^{\dagger 2} a_n^2 + \epsilon_n\left(a_n^{\dagger 2} + a_n^2\right), \tag{1}$$

where a_n ($a_n^\dagger$) is the annihilation (creation) operator of the cavity mode C_n and K_n denotes the Kerr-nonlinearity parameter of the cavity mode C_n. Assuming $K_n = K$, $\epsilon_n = \epsilon$, and $\epsilon = K\alpha^2$, the tensor products of coherent states $\{|\pm\alpha\rangle_1|\pm\alpha\rangle_2\cdots|\pm\alpha\rangle_N\}$ are the degenerate ground eigenstates of H_0 [67], where $|\pm\alpha\rangle_n$ denotes the coherence states with the amplitudes $\pm\alpha$ of the cavity mode C_n. When the condition $|\alpha| \gg 1$ is satisfied, both of the degenerate eigenstates $\{|\pm\alpha\rangle_1|\pm\alpha\rangle_2\cdots|\pm\alpha\rangle_N\}$ are approximately orthogonal. By setting appropriate parameters (which will be determined in the next section), the evolution of the system will be confined to the subspace composed of these degenerate eigenstates.

The auxiliary qutrit has three levels, $|g\rangle_q$, $|e\rangle_q$, and $|f\rangle_q$, as shown in Fig. 1. The transition frequencies of the transitions $|e\rangle_q \leftrightarrow |g\rangle_q$, $|f\rangle_q \leftrightarrow |e\rangle_q$, and $|f\rangle_q \leftrightarrow |g\rangle_q$ are ω_{eg}, ω_{fe}, and ω_{fg}, respectively. The transition $|e\rangle_q \leftrightarrow |f\rangle_q$ is resonantly coupled to the cavity mode C_n with coupling strength g_n. A pair of classical fields with the Rabi frequencies $\Omega_1(t)$ and $\Omega_2(t)$ are applied to the auxiliary qutrit to drive the transitions $|g\rangle_q \leftrightarrow |e\rangle_q$ and $|g\rangle_q \leftrightarrow |f\rangle_q$, respectively. Under the rotating-wave approximation, the interaction Hamiltonian of the qutrit is given by

$$\begin{aligned} H_1(t) &= H_c + H_q(t), \\ H_c &= \sum_{n=1}^{N} g_n a_n^\dagger |e\rangle_q\langle f| + \text{H.c.}, \\ H_q(t) &= \Omega_1(t)|g\rangle_q\langle e| + \Omega_2(t)|g\rangle_q\langle f| + \text{H.c.} \end{aligned} \tag{2}$$

Hence, the Hamiltonian of the whole system is $H(t) = H_0 + H_1(t)$. Assuming $\Omega_1(t) = \Omega_2(t) = \Omega(t)/\sqrt{2}$, $|\phi_\pm\rangle_q = (|e\rangle_q \pm |f\rangle_q)/\sqrt{2}$, $H_q(t)$ becomes

$$H_q'(t) = \Omega(t)|g\rangle_q\langle\phi_+| + \text{H.c.} \tag{3}$$

We define the closest energy gap between degenerate ground eigenstates $\{|\pm\alpha\rangle_1|\pm\alpha\rangle_2\cdots|\pm\alpha\rangle_N\}$ and other eigenstates of H_0 as E_{gap} [67], which can be obtained with numerical calculations. Moreover, cat-state qubits are defined as

$$|\mathcal{C}_\pm\rangle_n = \frac{1}{\sqrt{N_\pm}}(|\alpha\rangle_n \pm |-\alpha\rangle_n), \tag{4}$$

where $N_\pm = 2[1 \pm \exp(-2|\alpha|^2)]$ are normalization coefficients. The subspace composed of $\{|\mathcal{C}_\pm\rangle_n\}$ is called the cat-state subspace. When $E_{\text{gap}} \gg |g_n\alpha|$ is satisfied, the transition probability from $\{|\pm\alpha\rangle_1|\pm\alpha\rangle_2\cdots|\pm\alpha\rangle_N\}$ to other eigenstates is very small [67,71,72]. Thus, we

project the Hamiltonian $H_1(t)$ onto the cat-state subspace and obtain

$$\begin{aligned} H_1^c(t) &= H_c^c + H_q^c(t), \\ H_c^c &= \left[\sum_{n=1}^{N} g_n\alpha(|\Psi_+\rangle_n\langle\Psi_+| - |\Psi_-\rangle_n\langle\Psi_-|)\right] \\ &\quad\otimes(|\phi_+\rangle_q\langle\phi_+| - |\phi_-\rangle_q\langle\phi_-|), \\ H_q^c &= \Omega(t)\sum_{n=1}^{N}(|\Psi_+\rangle_n\langle\Psi_+| + |\Psi_-\rangle_n\langle\Psi_-|) \\ &\quad\otimes|g\rangle_q\langle\phi_+| + \text{H.c.}, \end{aligned} \tag{5}$$

where

$$|\Psi_\pm\rangle_n = \frac{1}{\sqrt{2}}(|\mathcal{C}_+\rangle_n \pm |\mathcal{C}_-\rangle_n). \tag{6}$$

To make the parity measurement more explicit, we introduce the parity operator of cat-state qubits as

$$P = \bigotimes_{n=1}^{N}\left\{\sum_{\iota=\pm}\iota|\Psi_\iota\rangle_n\langle\Psi_\iota|\right\}\otimes I_q, \tag{7}$$

where I_q is the unit operator of the qutrit. The even- and odd-parity states $|\varphi_{\text{even}}\rangle$ and $|\varphi_{\text{odd}}\rangle$ are the eigenstates of the parity operator P with eigenvalues 1 and -1, respectively. In other words, we have

$$P|\varphi_{\text{even}}\rangle = |\varphi_{\text{even}}\rangle, \quad P|\varphi_{\text{odd}}\rangle = -|\varphi_{\text{odd}}\rangle. \tag{8}$$

In addition, we define the operator

$$\mathcal{G}_{1,N}^{(j)} = \sum_{J=1}^{N_j}\left|\Phi_j^{(J)}\right\rangle_{1,N}\left\langle\Phi_j^{(J)}\right|, \tag{9}$$

where

$$\begin{aligned} \left|\Phi_j^{(J)}\right\rangle_{1,N} &= \mathcal{T}_j(J)|\Phi_s\rangle, \\ |\Phi_s\rangle &= |\underbrace{\Psi_+,\ldots,\Psi_+}_{N-j},\underbrace{\Psi_-,\ldots,\Psi_-}_{j}\rangle_{1,\ldots,N}, \end{aligned} \tag{10}$$

$|\Phi_s\rangle$ is the standard permutation state, $N_j = C_N^j$ is the sum of all possible permutations, and $\mathcal{T}_j(J)$ denotes the operator which turns the standard state $|\Phi_s\rangle$ into the Jth permutation state. Assuming that $g_n = g$ and α are real, the Hamiltonian in Eq. (5) reduces to

$$\begin{aligned} \mathcal{H}_1^c(t) &= \mathcal{H}_c^c + \mathcal{H}_q^c(t), \\ \mathcal{H}_c^c &= \sum_{j=0}^{N}(N-2j)g\alpha\mathcal{G}_{1,N}^{(j)}\otimes(|\phi_+\rangle_q\langle\phi_+| - |\phi_-\rangle_q\langle\phi_-|), \\ \mathcal{H}_q^c(t) &= \sum_{j=0}^{N}\Omega(t)\mathcal{G}_{1,N}^{(j)}\otimes|g\rangle_q\langle\phi_+| + \text{H.c.} \end{aligned} \tag{11}$$

Rotating $\mathcal{H}_1^c(t)$ with a unitary operator $R_c(t) = \exp(-i\mathcal{H}_c^c t)$ and setting

$$\Omega(t) = \sum_{m=0}^{[N/2]}\Omega_m(t)\exp(i\omega_m t), \quad \omega_m = (N-4m)\tilde{\omega}, \tag{12}$$

the Hamiltonian of the system becomes

$$\begin{aligned} \mathcal{H}_r^c(t) &= R_c^\dagger(t)\mathcal{H}_1^c(t)R_c(t) - iR_c^\dagger(t)\dot{R}_c(t) \\ &= \sum_{m=0}^{[N/2]}\Omega_m(t)\exp[i(N-4m)\tilde{\omega}t - i(N-2j)g\alpha t] \\ &\quad\times\sum_{j=0}^{N}\mathcal{G}_{1,N}^{(j)}\otimes|g\rangle_q\langle\phi_+| + \text{H.c.}, \end{aligned} \tag{13}$$

where $\tilde{\omega}$ is a time-independent parameter and $[N/2]$ is the integer floor function.

In order to realize a parity-selective qutrit transition, $\tilde{\omega} = g\alpha$ and $|\tilde{\omega}| \gg |\Omega_m(t)|$ are selected. Omitting the terms with high-frequency oscillations, the effective Hamiltonian of the system is derived as

$$H_e(t) = \sum_{m=0}^{[N/2]}\Omega_m(t)\mathcal{G}_{1,N}^{(2m)}\otimes|g\rangle_q\langle\phi_+| + \text{H.c.} \tag{14}$$

Assuming that the initial state of the qutrit is $|g\rangle_q$, under the control of the Hamiltonian $H_e(t)$, it is possible to drive the qutrit from the ground level $|g\rangle_q$ to the dressed state $|\phi_+\rangle_q$ when the cat-state qubits are in the even-parity states by designing proper Rabi frequency $\Omega_m(t)$. However, when the cat-state qubits are in the odd-parity states, the qutrit cannot be excited to the dressed state $|\phi_+\rangle_q$ and thus remains in its ground level $|g\rangle_q$. Therefore, we can determine the parity of N cat-state qubits by detecting the final population of the state $|g\rangle_q$ after a proper operation with operation time T.

The operation mentioned above can be realized by a flat π pulse, i.e., $\Omega_m(t) = \pi/2T$. However, if there is a systematic error in the coupling strength, i.e., $g \to g(1+\delta)$, a frequency mismatch will appear in the effective Hamiltonian, and the accuracy of the parity measurement may be greatly reduced. Hence, in order to enhance the robustness of the parity measurement against the systematic errors of the coupling strengths, an appropriate method is needed. Here, we exploit invariant-based reverse engineering and optimal control to find a proper evolution path and select proper control parameters, which will be described in the next section.

III. CONTROL-FIELD DESIGN

Supposing that $\{\Omega_m(t)\}$ are set so they are equal, i.e., $\Omega_m(t) = \Omega(t)$, the evolution governed by the effective Hamiltonian $H_e(t)$ in Eq. (14) can be studied in $M = 2^{N-1}$ two-level orthogonal subspaces possessing SU(2) dynamical structures with the same control fields $\Omega(t)$. The basis vectors of each two-level subspace can be written as $|\xi_1\rangle = |\Phi_{(2m)}^{(J)}\rangle_{1,N}\bigotimes|g\rangle_q$ and $|\xi_2\rangle = |\Phi_{(2m)}^{(J)}\rangle_{1,N}\bigotimes|\phi_+\rangle_q$, and the Pauli operators for the subspace are defined as

$$\begin{aligned} \sigma_x &= |\xi_1\rangle\langle\xi_2| + |\xi_2\rangle\langle\xi_1|, \\ \sigma_y &= -i|\xi_2\rangle\langle\xi_1| + i|\xi_1\rangle\langle\xi_2|, \\ \sigma_z &= |\xi_2\rangle\langle\xi_2| - |\xi_1\rangle\langle\xi_1|, \end{aligned} \tag{15}$$

which satisfy the commutation relations

$$[\sigma_x,\sigma_y] = 2i\sigma_z, \quad [\sigma_y,\sigma_z] = 2i\sigma_x, \quad [\sigma_z,\sigma_x] = 2i\sigma_y. \tag{16}$$

The effective Hamiltonian in the two-level subspace reads

$$H^J_{(2m)}(t) = \Omega(t)\left|\Phi^{(J)}_{(2m)}\right\rangle_{1,N}\left\langle\Phi^{(J)}_{(2m)}\right| \otimes |g\rangle_q\langle\phi_+| + \text{H.c.}$$
$$= \Omega_x(t)\sigma_x + \Omega_y(t)\sigma_y + 0\times\sigma_z, \tag{17}$$

with $\Omega_x(t) = \text{Re}[\Omega(t)]$ and $\Omega_y(t) = \text{Im}[\Omega(t)]$.

To study the evolution in the two-level subspace by invariant-based reverse engineering, we should first find a dynamical invariant $I(t)$ fulfilling [77,78]

$$i\frac{\partial}{\partial t}I(t) - \left[H^J_{(2m)}(t), I(t)\right] = 0. \tag{18}$$

Since the Hamiltonian in Eq. (17) has a SU(2) dynamical structure [79–82], the dynamical invariant is found to be

$$I(t) = \sin\theta\cos\beta\,\sigma_x + \sin\theta\sin\beta\,\sigma_y + \cos\theta\,\sigma_z, \tag{19}$$

where θ and β are two time-dependent parameters.

By reverse solving Eq. (18), the expressions for $\Omega_x(t)$ and $\Omega_y(t)$ are

$$\Omega_x(t) = (\dot\beta\tan\theta\sin\beta - \dot\theta\cos\beta)/2,$$
$$\Omega_y(t) = (\dot\beta\tan\theta\cos\beta + \dot\theta\sin\beta)/2. \tag{20}$$

The eigenvectors of the dynamical invariant $I(t)$ are

$$|\zeta_+(t)\rangle = e^{i\beta/2}\cos\tfrac{\theta}{2}|\xi_1\rangle + ie^{-i\beta/2}\sin\tfrac{\theta}{2}|\xi_2\rangle,$$
$$|\zeta_-(t)\rangle = ie^{i\beta/2}\sin\tfrac{\theta}{2}|\xi_1\rangle + e^{-i\beta/2}\cos\tfrac{\theta}{2}|\xi_2\rangle, \tag{21}$$

with the eigenvalues ±1. Using the eigenvectors $|\zeta_\pm(t)\rangle$, two orthogonal solutions $|\psi_\pm(t)\rangle$ of the Schrödinger equation $i|\dot\psi(t)\rangle = H_e(t)|\psi(t)\rangle$ are derived as follows:

$$|\psi_\pm(t)\rangle = e^{i\mu_\pm(t)}|\zeta_\pm(t)\rangle, \tag{22}$$

where $\mu_\pm(t)$ are the Lewis-Riesenfeld phases [77,83], given by

$$\mu_\pm(t) = \langle\zeta_\pm(t)|\left[i\frac{\partial}{\partial t} - H^J_{(2m)}(t)\right]|\zeta_\pm(t)\rangle$$
$$= \mp\int_0^t \frac{\dot\beta(t')}{2\cos[\theta(t')]}dt'. \tag{23}$$

Here, we select the evolution paths $|\psi_+(t)\rangle$ to realize the evolution $|\psi_+(0)\rangle = |\xi_1\rangle \to |\psi_+(T)\rangle = e^{i\chi(T)/2}|\xi_2\rangle$. Then, the corresponding boundary conditions can be specified as

$$\theta(0) = \beta(0) = \beta(T) = 0, \quad \theta(T) = \pi. \tag{24}$$

So far, we have obtained expressions for the classical fields $\{\Omega_m(t)\}$ by using reverse engineering. However, to enhance the robustness against the systematic errors in the coupling strengths $\{g_n\}$, we need to further design the control parameters θ and β using optimal control.

Considering the systematic errors of the coupling strengths with systematic-error rate δ, i.e., $g \to g(1+\delta)$, the effective Hamiltonian in Eq. (13) becomes $H_s(t) = \mathcal{H}_e(t) + \delta\mathcal{H}^c_c$. The projection of the Hamiltonian $H_s(t)$ in the two-level subspace spanned by $\{|\xi_1\rangle, |\xi_2\rangle\}$ is written as

$$\tilde H^{(m)}_s(t) = H^J_{(2m)}(t) + \tilde H^{(m)}_\varsigma,$$
$$\tilde H^{(m)}_\varsigma = (N-4m)\delta g\alpha|\xi_2\rangle\langle\xi_2|$$
$$= \tfrac{1}{2}(N-4m)\delta g\alpha(\sigma_z - I) = \varsigma(\sigma_z - I), \tag{25}$$

where $I = |\xi_1\rangle\langle\xi_1| + |\xi_2\rangle\langle\xi_2|$ and $\varsigma = \frac{1}{2}(N-4m)\delta g\alpha$. By using the time-dependent perturbation theory, we get [75,84]

$$|\psi_\varsigma(T)\rangle = |\psi(T)\rangle - i\int_0^T dtU_0(T,t)\tilde H^{(m)}_\varsigma|\psi(t)\rangle + O(\varsigma^2),$$

where $U_0(T,t) = \sum_{l=\pm}|\psi_l(T)\rangle\langle\psi_l(t)|$ is the unperturbed time evolution operator, $O(\varsigma^2)$ are terms with order equal to or greater than ς^2, and $|\psi_\varsigma(t)\rangle$ ($|\psi(t)\rangle$) is the state of the system with (without) systematic errors.

The fidelity of the evolution $|\xi_1\rangle \to |\xi_2\rangle$ along paths $|\psi_+(t)\rangle$ can be approximately calculated as

$$F \approx 1 - \left|\frac{1}{T}\int_0^T \langle\psi_-(t)|\tilde H_\varsigma|\psi_+(t)\rangle dt\right|^2$$
$$= 1 - \varsigma^2\left|\frac{1}{T}\int_0^T e^{i\chi(t)}\sin\theta dt\right|^2, \tag{26}$$

with $\chi(t) = 2\mu_+(t)$. According to Refs. [75,76], the systematic-error sensitivity can be calculated as

$$Q = -\frac{1}{2}\frac{\partial^2 F}{\partial\varsigma^2}\Big|_{\varsigma=0} = \left|\frac{1}{T}\int_0^T e^{i\chi(t)}\sin\theta dt\right|^2. \tag{27}$$

To nullify the systematic-error sensitivity, we assume $\chi(t) = -(2\theta + 2\lambda\sin 2\theta)$ with an undetermined coefficient λ [76,85,86]. Using the relation $\chi(t) = 2\mu_+(t)$, we derive

$$\dot\chi(t) = -[2\dot\theta(1+2\lambda\cos 2\theta)] = -\dot\beta/\cos\theta$$
$$\Rightarrow \dot\beta(t) = 2\dot\theta\cos\theta(1+2\lambda\cos 2\theta). \tag{28}$$

According to the boundary conditions in Eq. (24), the expression for β is given by

$$\beta(t) = 2(1+2\lambda)\sin\theta - \frac{8\lambda}{3}\sin^3\theta. \tag{29}$$

Substituting $\beta(t)$ in Eq. (29) into Eq. (20), the specific expressions for the control fields can be obtained as

$$\Omega_x(t) = \frac{\dot\theta}{2}[2(1+2\lambda\cos 2\theta)\sin\beta\sin\theta - \cos\beta],$$
$$\Omega_y(t) = \frac{\dot\theta}{2}[2(1+2\lambda\cos 2\theta)\cos\beta\sin\theta + \sin\beta]. \tag{30}$$

In addition, based on the boundary conditions in Eq. (24), the parameter $\theta(t)$ can be selected as

$$\theta(t) = \pi\sin^2(\pi t/2T). \tag{31}$$

After numerical calculations, a solution $\lambda = -0.2058$ for $Q \simeq 0$ is found, and the wave shapes of $\Omega_x(t)$ and $\Omega_y(t)$ can be obtained and are shown in Fig. 2.

IV. NUMERICAL SIMULATIONS

In this section, let us estimate the performance of the protocol via numerical simulations. In the numerical simulations, we take the even- and odd-parity states of the N cat-state

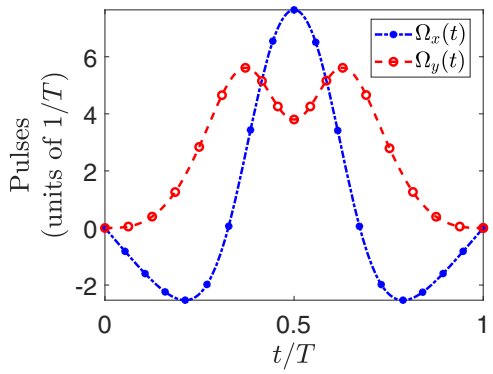

FIG. 2. The control fields $\Omega_x(t)$ and $\Omega_y(t)$ versus t/T.

qubits

$$|\varphi_{\text{even}}\rangle = 2^{(1-N)/2}\sum_{m=0}^{[N/2]}\sum_{J=1}^{N_{2m}}\left|\Phi_j^{(J)}\right\rangle_{1,N},$$
$$|\varphi_{\text{odd}}\rangle = 2^{(1-N)/2}\sum_{m=0}^{[N/2]}\sum_{J=1}^{N_{2m+1}}\left|\Phi_j^{(J)}\right\rangle_{1,N} \quad (32)$$

as examples. In addition, the initial state of the superconducting qutrit is prepared in the ground level $|g\rangle_q$.

A. Verification of the protocol for different numbers of cat-state qubits

In Sec. III, the control fields were designed using the two-level effective Hamiltonian in Eq. (17). In order to examine the validity of the protocol, we study the evolution of the system under the control of the full Hamiltonian $H(t)$ defined below Eq. (2) in Sec. II. When the system is controlled by the full Hamiltonian, the evolution is governed by the equation

$$\dot{\rho}(t) = -i[H(t), \rho(t)], \quad (33)$$

where $\rho(t)$ is the density operator of the total system. We choose the Kerr-nonlinearity parameter $K = 2\pi \times 12.5$ MHz, the amplitude $\alpha = 2$ of the coherent state, the operation time $T = 5$ μs, and the coupling strength $g_n = g = 5$ MHz to perform numerical simulations. With the selected parameters, we have $E_{\text{gap}} = 1038.1$ MHz. Thus, the condition $E_{\text{gap}} \gg |g_n\alpha|$ is well satisfied, and the cavity mode C_n is restricted in the cat-state subspace. The population of the states $|g\rangle_q$ and $|\phi_+\rangle_q$ at time t are defined as

$$P_g(t) = \text{Tr}[\rho(t)|g\rangle_q\langle g|], \quad P_\phi(t) = \text{Tr}[\rho(t)|\phi_+\rangle_q\langle\phi_+|].$$

The number of cat-state qubits is selected to be $N = 2, 3, 4$ to verify the validity of the protocol. When the cavity states are in the even- or odd-parity states, the corresponding initial states of the whole system are, respectively,

$$|\phi_o\rangle = |\varphi_{\text{even}}\rangle \otimes |g\rangle_q, \quad |\phi_e\rangle = |\varphi_{\text{even}}\rangle \otimes |g\rangle_q. \quad (34)$$

For different initial states $|\phi_o\rangle$ and $|\phi_e\rangle$, the populations $P_g(t)$ and $P_\phi(t)$ versus t are plotted in Figs. 3(a), 3(b), and 3(c) for $N = 2, N = 3$, and $N = 4$, respectively. The values of $\{P_g(T), P_\phi(T)\}$ for $N = 2, 3, 4$ are listed in Table I. From Fig. 3 and Table I, we find $\{P_g(T), P_\phi(T)\} \approx \{0, 1\}$ $[\{P_g(T), P_\phi(T)\} \approx \{1, 0\}]$ for the case of even (odd) parity. This means that the final state of the auxiliary qutrit is $|g\rangle_q$ ($|\phi_+\rangle_q$) for the odd- (even-) parity case. Thus, the parity-selective qutrit transition is successfully realized. We can distinguish the parity of the cat-state qubits by measuring the final state of the qutrit.

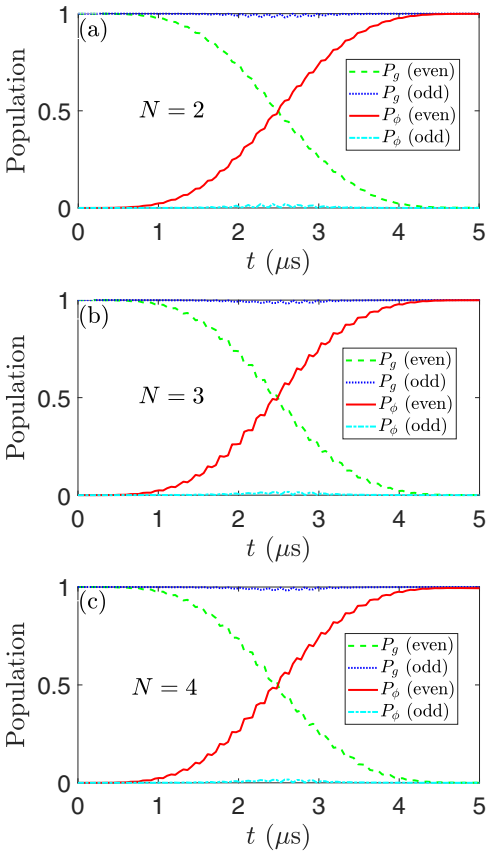

FIG. 3. The populations $P_g(t)$ and $P_\phi(t)$ versus t for the (a) $N = 2$, (b) $N = 3$, and (c) $N = 4$ cases.

B. Optimization of the protocol by selecting the proper coupling strength and operation time

Generally speaking, the influence of decoherence increases when the operation time T increases. Hence, a shorter operation time is better to reduce the influence of decoherence. However, according to Eqs. (30) and (31), a shorter operation time T means that a stronger control field $\Omega_m(t)$ is needed. If the amplitude of the control field $\Omega_m(t)$ is relatively large and the coupling strength g remains unchanged, the condition $|\tilde{\omega}| \gg |\Omega_m(t)|$ ($\tilde{\omega} = g\alpha$) cannot be not well satisfied. The desired evolution of the system will be destroyed. In fact,

TABLE I. The values of $\{P_g(T), P_\phi(T)\}$ for $N = 2, 3, 4$.

	N		
	2	3	4
$P_g(T)$ (even)	9.2541×10^{-4}	5.2936×10^{-4}	5.2900×10^{-4}
$P_\phi(T)$ (even)	0.9991	0.9993	0.9938
$P_g(T)$ (odd)	1.0000	1.0000	1.0000
$P_\phi(T)$ (odd)	0.0000	8.8175×10^{-6}	8.7974×10^{-6}

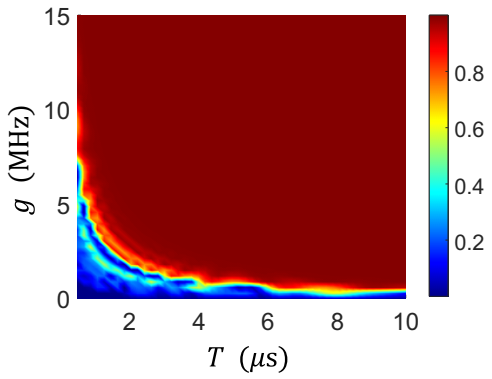

FIG. 4. The distinguishability $D(T)$ versus the coupling strength g and the operation time T.

the satisfaction of the condition $|\tilde{\omega}| \gg |\Omega_m(t)|$ becomes better with an increasing value of g, but the condition $E_{\text{gap}} \gg |g_n\alpha|$ may be broken with the increase of the coupling strength g. Because the value of the Kerr-nonlinear coefficient K is finite in experiments, it is better to keep the Kerr-nonlinear coefficient K unchanged for the sake of experimental feasibility. Hence, we should strike a balance between the values of g and T.

To estimate the performance of the protocol, we define the distinguishability of the even- and odd-parity states as

$$D(t) = \left|P_g^e(t) - P_g^o(t)\right|. \tag{35}$$

The populations of the ground level $|g\rangle_q$ in the even- (odd-) parity cases are given by

$$P_g^e(t) = \text{Tr}[\rho_e(t)|g\rangle_q\langle g|], \quad P_g^o(t) = \text{Tr}[\rho_o(t)|g\rangle_q\langle g|], \tag{36}$$

respectively, where $\rho_e(t)$ [$\rho_o(t)$] is the density operator of the system at time t with the initial state $|\phi_e\rangle$ ($|\phi_o\rangle$). When the value of $D(T)$ is closer to 1, the parity of the cat-state qubits can be better distinguished by measuring the population of the ground state of the qutrit.

Considering the case of $N = 3$, the distinguishability $D(T)$ versus the coupling strength g and the operation time T is plotted in Fig. 4, where the value of distinguishability $D(T)$ is greater than 0.99 when the coupling strength $g \geqslant 10$ MHz and the operation time $T \geqslant 0.7$ μs. We can select $g = 10$ MHz and $T = 1$ μs for an acceptable distinguishability of 0.9967. In the following numerical simulations, we take $N = 3$ as an example and fix $g = 10$ MHz and $T = 1$ μs to estimate the performance of the protocol in the presence of different disturbing factors.

We also studied the performance of the protocol by considering cat-state qubits with different coherent-state amplitudes α. The distinguishability $D(T)$ versus the amplitude α ($\alpha \in [0.5, 3]$) is shown in Fig. 5(a). As shown by Fig. 5(a), the distinguishability $D(T)$ is greater than 0.99 and tends to be stable for $\alpha \geqslant 1.67$. This means the protocol can be well performed over a wide range of amplitude α. The performance of the protocol is nearly perfect when α is large enough because a larger amplitude α can satisfy the condition $E_{\text{gap}} \gg |g_n\alpha|$ better because $E_{\text{gap}} \simeq 4K\alpha^2$ [67], which greatly reduces the probability of leakage from the cat-state subspace to other eigenstates. This agrees with the theoretical analysis in Sec. II.

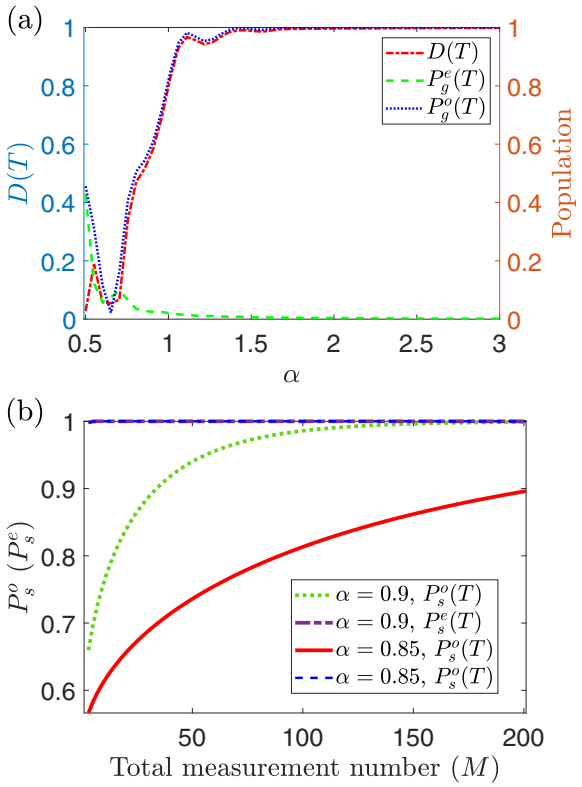

FIG. 5. (a) The distinguishability $D(T)$ and the populations $P_g^o(T)$ and $P_g^e(T)$ of the auxiliary qutrit in the odd- and even-parity cases versus the amplitude α of the coherent state. (b) The successful probabilities $P_s^o(T)$ and $P_s^e(T)$ versus the total measurement number M of the repeated measurements.

We consider the fact that a large α can affect the cat-state qubits mainly through bit-flip errors, while the phase-flip errors are exponentially suppressed [67] (see Sec. IV G). The large-amplitude cat-state qubits may be promising candidates for quantum information processing [59]. Therefore, the protocol may be helpful for quantum information processing based on large-amplitude cat-state qubits.

As the small-amplitude cat-state qubits can also be used in quantum information processing [68], we also study the performance of the protocol in cases where the amplitudes of the cat-state qubits are relatively small. We can see from Fig. 5(a) that the distinguishability $D(T)$ remains higher than 0.942 when $\alpha \geqslant 1.1$. This means that the protocol still produces relatively high distinguishability when the average photon number of the cat-state qubit is near 1. However, when $\alpha \leqslant 1$, the distinguishability $D(T)$ tends to decrease more shapely. This may be detrimental to the implementation of the protocol. When $\alpha \geqslant 0.85$, the distinguishability $D(T)$ is still higher than 0.516. Thus, in the case of $\alpha \geqslant 0.85$, the successful probability of the protocol can still be enhanced by repeated measurements. As the parity of the cat-state qubits remains unchanged after the whole process, to repeat the measurement, one should just reinitialize the auxiliary qutrit to its lowest level $|g\rangle_q$. We assume that the final measurement result is decided by which of the two parities is reported more times in M ($M = 1, 3, 5, \ldots$) repeated measurements. Consequently, for odd- and even-parity states, the final successful

probabilities are, respectively, given by

$$P_s^o(T) = \sum_{J=(M+1)/2}^{M} C_M^J \left[P_g^o(T)\right]^J \left[1 - P_g^o(T)\right]^{M-J},$$

$$P_s^e(T) = \sum_{J=(M+1)/2}^{M} C_M^J \left[1 - P_g^e(T)\right]^J \left[P_g^e(T)\right]^{M-J}. \quad (37)$$

Here, $P_g^o(T)$ and $P_g^e(T)$ are the populations of the lowest level $|g\rangle_q$ of the auxiliary qubit at time T in the odd- and even-parity cases. Taking $\alpha = 0.85$ as an example, in the odd- and even-parity cases, we obtain $P_g^o(T) = 0.5443$ and $P_g^e(T) = 0.0281$, respectively. The successful probabilities $P_s^o(T)$ and $P_s^e(T)$ versus the total measurement number M of the repeated measurements are shown in Fig. 5(b). As shown by the red solid and blue dashed curves, the successful probabilities $P_s^o(T)$ and $P_s^e(T)$ both increase with the increase of the total measurement number M. The successful probability $P_s^e(T)$ is near unity, while the successful probability $P_s^o(T)$ can be higher than 0.8 when $M \geqslant 91$. For $\alpha = 0.9$, we have $P_g^o(T) = 0.6081$ and $P_g^e(T) = 0.0247$. The successful probabilities $P_s^o(T)$ and $P_s^e(T)$ versus the total measurement number M are shown by the green dotted and purple dashed-dotted curves. We can see that the successful probability $P_s^o(T)$ can be enhanced to 0.9 with only $M = 35$. Hence, multiple measurements can improve the successful probability for distinguishing the two parities in the case of small α. In this paper we still focus on the performance of the protocol at one measurement. Therefore, in the following discussion, as an example to further estimate the performance of the protocol, we consider a moderate value of the amplitude, $\alpha = 2$.

C. Effects of systematic errors on the protocol

We now estimate the performance of the protocol under the influence of systematic errors and compare the results with those for the protocol using a flat π pulse. First, let us consider the systematic errors of the coupling strength g. In this case, the coupling strength g becomes $g(1 + \delta)$ with the systematic-error rate δ. The distinguishability $D(T)$ versus the systematic-error rate δ is plotted in Fig. 6(a). For both protocols using the time-dependent pulses designed in Sec. III and the flat π pulse, the distinguishability $D(T)$ decreases as $|\delta|$ increases for the systematic-error rate $\delta \in [-0.1, 0.1]$. Especially, for the flat π-pulse case, the value of $D(T)$ falls below 90% for $|\delta| \geqslant 0.008$. The value of $D(T)$ is equal to or greater than 98% only when $\delta \in [-0.004, 0.004]$. However, for the time-dependent pulse case, the value of $D(T)$ is always greater than 90% when $\delta \in [-0.1, 0.1]$, and the value of $D(T)$ is equal to or greater than 98% for $\delta \in [-0.096, 0.076]$. From the above data, we can see that the distinguishability is very sensitive to the systematic errors of the coupling strengths when using the flat π pulse but robust against the systematic errors of the coupling strengths when utilizing the time-dependent pulse.

Now we investigate the systematic errors of the classical fields. In fact, if the classical fields have systematic errors, the Rabi frequency will become $\Omega_m(t) \to (1 + \bar{\delta})\Omega_m(t)$, where $\bar{\delta}$ is the error rate. In order to study the performance of the protocol in the presence of systematic errors in the control fields, in Fig. 6(b), we plot the distinguishability $D(T)$ versus the systematic-error rate $\bar{\delta} \in [-0.2, 0.2]$ for both protocols with the flat π pulse and the time-dependent pulse $\Omega_m(t)$ designed in Sec. III. As shown in Fig. 6(b), the distinguishability $D(T)$ decreases as $|\bar{\delta}|$ increases. The value of $D(T)$ is only about 89% when $\bar{\delta}$ reaches -0.2 using the flat π pulse. For the time-dependent pulse, the values of $D(T)$ are always equal to or greater than 97.5% when $\bar{\delta} \in [-0.2, 0.2]$. This demonstrates that the protocol with the time-dependent pulse is also insensitive to the systematic errors of the control fields.

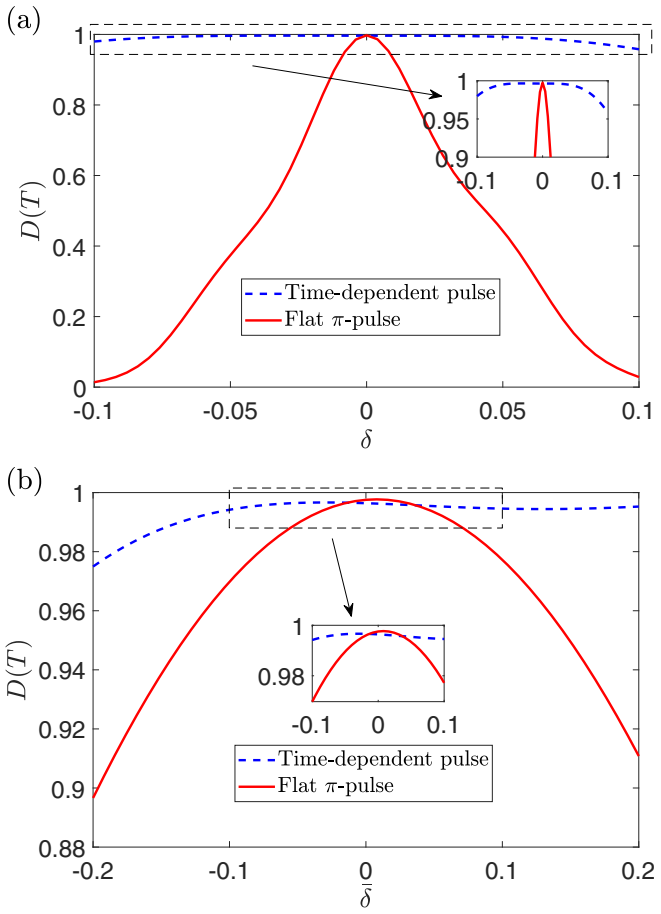

FIG. 6. (a) The distinguishability $D(T)$ versus the systematic-error rate δ for the flat π pulse and the time-dependent pulse. (b) The distinguishability $D(T)$ versus the systematic-error rate $\bar{\delta}$ for the flat π pulse and the time-dependent pulse.

Now we compare the influence of the systematic errors of the coupling strengths with that of the classical fields. As shown by the blue dashed (red solid) line in the insets of Figs. 6(a) and 6(b), the distinguishability $D(T)$ in the inset of Fig. 6(a) decreases more sharply than the distinguishability $D(T)$ in the inset of Fig. 6(b) when the error rates increase. This is because the systematic errors of the coupling strengths will cause a frequency mismatch in the effective Hamiltonian, which destroys the parity-selective qutrit transition. Especially in the case of the flat π pulse, the distinguishability $D(T)$ is very sensitive to the systematic errors of the coupling strengths. Therefore, the systematic errors of the coupling strengths have greater influence than the systematic errors of

the classical fields. This is why we should design and select proper evolution paths and control parameters using reverse engineering and optimal control to enhance the robustness against the systematic errors of the coupling strengths.

D. Effects of the inhomogeneity of coupling strengths on the protocol

In a real implementation of the protocol, all the coupling strengths $\{g_n\}$ cannot be completely equal. To evaluate the performance of the protocol under the influence of the inhomogeneity of the coupling strengths, we choose $N = 3$ as an example. The coupling strengths of the three cavities of the auxiliary qutrit are set as $g_1 = g(1+\delta_1)$, $g_2 = g(1+\delta_2)$, and $g_3 = g$, where δ_1 and δ_2 are the deviation rates. We numerically simulate the distinguishability $D(T)$ versus the deviation rates δ_1 and δ_2. As shown in Fig. 7(a), when the deviation rates are $\delta_1 \in [-0.1, 0.1]$ and $\delta_2 \in [-0.1, 0.1]$, the values of $D(T)$ decrease as the values of $|\delta_1|$ and $|\delta_2|$ increase. However, the values of $D(T)$ are always greater than or equal to 98.14%. This indicates that the protocol is insensitive to the inhomogeneity of the coupling strengths.

E. Effects of intercavity cross talk on the protocol

In the experimental implementation, cross talk between the cavities is inevitable [87], which will affect the evolution of the system. When the cavity number N is equal to 3, the intercavity cross talk is described as

$$H_{\rm cr} = g_{12}a_1^\dagger a_2 + g_{23}a_2^\dagger a_3 + g_{13}a_1^\dagger a_3 + \text{H.c.}, \tag{38}$$

where g_{12}, g_{23}, and g_{13} are the cross-talk coupling strengths. When the cross talk is taken into account, the Hamiltonian of the system is $H_r(t) = H(t) + H_{\rm cr}$, and the evolution of the system can be described by the equation

$$\dot{\rho}(t) = -i[H_r(t), \rho(t)]. \tag{39}$$

The cross-talk coupling strengths $g_{12} \in [0, 0.1g]$, $g_{23} \in [0, 0.1g]$, and $g_{13} = 0$ are selected to test the performance of the protocol. We plot the distinguishability $D(T)$ versus coupling strengths g_{12} and g_{23} in Fig. 7(b). As shown in Fig. 7(b), the distinguishability $D(T)$ decreases with the increase of the cross-talk coupling strengths. However, for $g_{12} \in [0, 0.1g]$ and $g_{23} \in [0, 0.1g]$, the values of $D(T)$ are always greater than 99.6%. This means that the effect of cavity cross talk on the protocol can be ignored. In fact, the states of the cavities are restricted in the cat-state subspace due to strong Kerr nonlinearity, which makes the protocol insensitive to the cavity cross talk. Moreover, because the intercavity cross talk $H_{\rm cr}$ and the parity operator of the cavities P in Eq. (7) are commutated, the intercavity cross talk $H_{\rm cr}$ does not change the parity of the cavities. That is why the effect of cavity cross talk can be ignored.

F. Effects of anharmonicity on the protocol

During the realization of the protocol, the couplings between the qutrit and the cavities and the classical fields applied to the qutrit will cause unwanted transitions. When the transition frequencies of the unwanted transitions and the transition

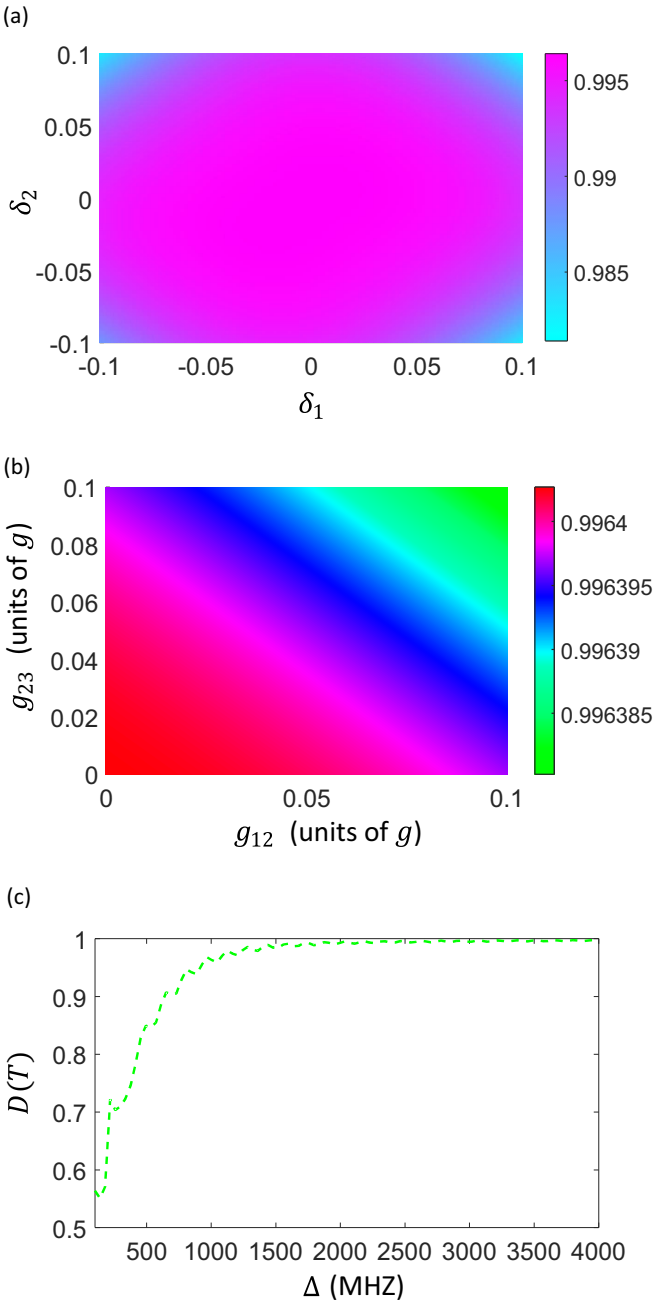

FIG. 7. (a) The distinguishability $D(T)$ versus the deviation rate δ'. (b) The distinguishability $D(T)$ versus the cross-talk coupling strengths g' (in units of g). (c) The distinguishability $D(T)$ versus the detuning Δ.

frequencies of the wanted transitions are close, the unwanted transitions may have a large influence on the protocol. For example, because the values of ω_{fe} and ω_{eg} are relatively close, (1) the unwanted coupling between the transition $|g\rangle_q \leftrightarrow |e\rangle_q$ and the cavity mode C_n with the detuning $\Delta_n = |\omega_{fe} - \omega_{eg}|$ and (2) the unwanted driving $|f\rangle_q \leftrightarrow |e\rangle_q$ with the detuning $\Delta' = |\omega_{fe} - \omega_{eg}|$ should be considered. The unwanted coupling between the transition $|g\rangle_q \leftrightarrow |f\rangle_q$ and the cavity mode C_n can be ignored because the transition frequencies satisfy $\omega_{fg} \gg \omega_{fe}$. Taking unwanted transitions 1 and 2 into account, the Hamiltonian of the system is $H_r(t) = H(t) +$

$H_d(t)$, where the Hamiltonian $H_d(t)$ is described by

$$H_d(t) = \left(\sum_{n=1}^{N} g_n a_n e^{i\Delta_n t}\right) \otimes |e\rangle_q\langle g| + \Omega(t)e^{i\Delta' t} \otimes |e\rangle_q\langle f| + \text{H.c.} \quad (40)$$

To evaluate the effect of unwanted transitions on the protocol, we numerically simulate the distinguishability $D(T)$ versus the detuning $\Delta_n = \Delta' = \Delta$. As shown in Fig. 7(c), the value of $D(T)$ increases when the value of Δ increases. When $\Delta \in [100, 4000]$ MHz [88], it is worth noting that the distinguishability $D(T) \geqslant 90\%$ for detuning $\Delta \in [650, 4000]$ MHz. This suggests that the protocol works well when the superconducting qutrit has strong anharmonicity. Therefore, to ensure the effectiveness of the protocol, we should preferably choose a superconducting qutrit with strong anharmonicity. For example, a flux qutrit or charge qutrit, whose anharmonicity can reach the order of gigahertz [88–91], is suitable to implement the protocol.

G. Effects of decoherence on the protocol

Since the system cannot be completely separated from the environment, decoherence of the system will occur. Thus, the influence of environment-induced decoherence should also be taken into account. The main decoherent factors in the protocol are the dephasing from levels $|e\rangle_q$ and $|f\rangle_q$; the qutrit energy relaxation for relaxation paths $|f\rangle_q \to |e\rangle_q$, $|f\rangle_q \to |g\rangle_q$, and $|e\rangle_q \to |g\rangle_q$; and the single-photon loss of each cavity. The evolution of the system in the presence of decoherence can be described by the Lindblad master equation [59,92],

$$\dot{\rho}(t) = -i[H(t), \rho(t)] + \sum_{k=e,f} \gamma_{kk}\mathcal{L}[\sigma_{kk}] + \gamma_{fg}\mathcal{L}[\sigma_{fg}^{-}] + \gamma_{fe}\mathcal{L}[\sigma_{fe}^{-}] + \gamma_{eg}\mathcal{L}[\sigma_{eg}^{-}] + \sum_{n=1}^{N} \kappa_n \mathcal{L}[a_n], \quad (41)$$

where $\sigma_{kk} = |k\rangle_q\langle k|$, $\sigma_{fg}^{-} = |g\rangle_q\langle f|$, $\sigma_{fe}^{-} = |e\rangle_q\langle f|$, $\sigma_{eg}^{-} = |g\rangle_q\langle e|$, and $\mathcal{L}[O] = O\rho(t)O^{\dagger} - O^{\dagger}O\rho(t)/2 - \rho(t)O^{\dagger}O/2$, with $O = \sigma_{kk}, \sigma_{fg}^{-}, \sigma_{fe}^{-}, \sigma_{eg}^{-}, a_n$. Here, γ_{kk} is the dephasing rate, γ_{fg} (γ_{fe}, γ_{eg}) is the qutrit spontaneous emission rate, and κ_n is the single-photon loss rate of the cavity. For simplicity, we set $\gamma_{kk} = \Gamma$, $\gamma_{fg} = \gamma_{fe} = \gamma_{eg} = \gamma$, and $\kappa_n = \kappa$ in following numerical simulations.

We numerically simulate the distinguishability $D(T)$ versus the dephasing rates (the single-photon loss rates of three cavities) and the spontaneous emission rates in Fig. 8(a) [Fig. 9(a)]. We define the projection operator of the cat-state subspace as

$$P_{\text{cat}} = \sum_{n=1}^{N} |\Psi_+\rangle_n\langle\Psi_+| + |\Psi_-\rangle_n\langle\Psi_-|. \quad (42)$$

The probability of leakage from the cat-state subspace P_{L} versus the dephasing rates (the single-photon loss rates of three cavities) and the spontaneous emission rates is shown in Figs. 8(b) and 8(c) [Figs. 9(b) and 9(c)] for different initial states $|\phi_e\rangle$ and $|\phi_o\rangle$. Here, we have $P_{\text{L}} = 1 - \text{Tr}[\rho_{e(o)}(T)P_{\text{cat}}]$.

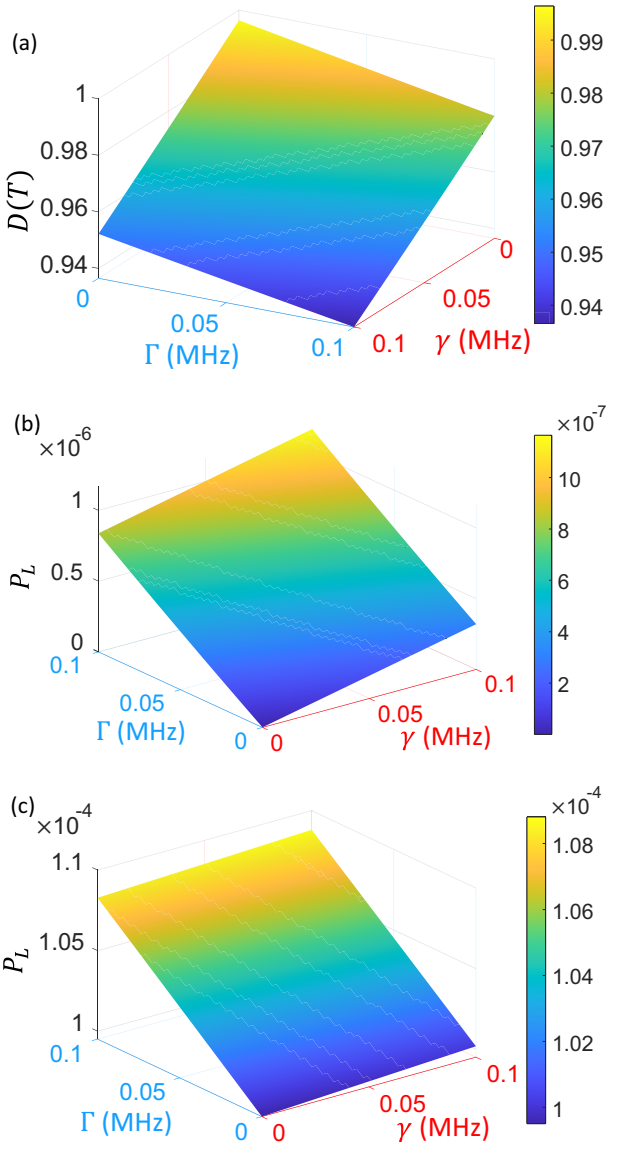

FIG. 8. (a) The distinguishability $D(T)$ versus the dephasing rates $\Gamma \in [0, 0.1]$ MHz and the spontaneous emission rates $\gamma \in [0, 0.1]$ MHz. (b) The probability of leakage from the cat-state subspace P_{L} versus the dephasing rates $\Gamma \in [0, 0.1]$ MHz and the spontaneous emission rates $\gamma \in [0, 0.1]$ MHz for the initial state $|\phi_e\rangle$. (c) The probability of leakage from the cat-state subspace P_{L} versus the dephasing rates $\Gamma \in [0, 0.1]$ MHz and the spontaneous emission rates $\gamma \in [0, 0.1]$ MHz for the initial state $|\phi_o\rangle$. In all plots, $\kappa = 0$ is set.

Figure 8(a) shows that the protocol can achieve the distinguishability $D(T) \geqslant 93.6\%$ for $\Gamma \in [0, 0.1]$ MHz and $\gamma \in [0, 0.1]$ MHz ($\kappa = 0$). Figure 9(a) shows that the protocol can achieve the distinguishability $D(T) \geqslant 95.2\%$ for $\gamma \in [0, 0.1]$ MHz and $\kappa \in [0, 0.01]$ MHz ($\Gamma = 0$) [89,93–95]. From Figs. 8(a) and 9(a), we can see that the spontaneous emission is the main factor affecting the protocol. However, the protocol can still produce distinguishability [$D(T) \geqslant 95.2\%$] in the presence of the spontaneous emission. Thus, the protocol is somewhat robust to decoherence.

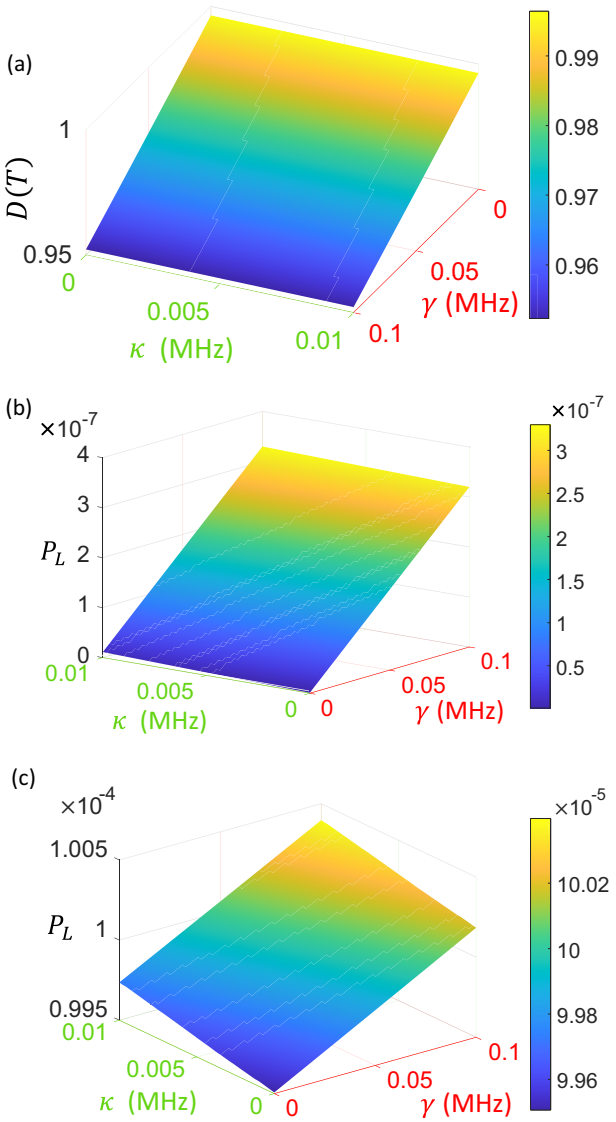

FIG. 9. (a) The distinguishability $D(T)$ versus the single-photon loss rates $\kappa \in [0, 0.01]$ MHz and the spontaneous emission rates $\gamma \in [0, 0.1]$ MHz. (b) The probability of leakage from the cat-state subspace $P_{\rm L}$ versus the single-photon loss rates $\kappa \in [0, 0.01]$ MHz and the spontaneous emission rates $\gamma \in [0, 0.1]$ MHz for the initial state $|\phi_e\rangle$. (c) The probability of leakage from the cat-state subspace $P_{\rm L}$ versus the single-photon loss rates $\kappa \in [0, 0.01]$ MHz and the spontaneous emission rates $\gamma \in [0, 0.1]$ MHz for the initial state $|\phi_o\rangle$. In all plots, $\Gamma = 0$ is set.

In Figs. 8(b) and 8(c) [Figs. 9(b) and 9(c)], we can see that the probability of leakage $P_{\rm L}$ is always less than 1.2×10^{-6} and 1.1×10^{-4} (3.3×10^{-7} and 1.005×10^{-4}) for initial states $|\phi_e\rangle$ and $|\phi_o\rangle$. This indicates that the cavity states barely leak to other states and almost stay in the cat-state subspace throughout the evolution process. This is because the single-photon loss of the cavities is equivalent to a bit flip σ_n^x within the cat-state subspace under a strong two-photon squeezing drive [59,63,67]. Specifically, the Lindblad operator $\mathcal{L}[a_n]$ in the eigenstate subspace of the Hamiltonian H_0 is written as

$$\begin{aligned}\mathcal{L}[a_n] \simeq{}& \alpha^2\mathcal{L}[\sqrt{\tanh\alpha^2}|\mathcal{C}_+\rangle_n\langle\mathcal{C}_-| + \sqrt{\coth\alpha^2}|\mathcal{C}_-\rangle_n\langle\mathcal{C}_+|] \\ &+ \mathcal{L}\left[\sqrt{\frac{N_+}{N_+^e}}|\mathcal{C}_+\rangle_n\langle\ominus_+^e| + \sqrt{\frac{N_-}{N_-^e}}|\mathcal{C}_-\rangle_n\langle\ominus_-^e|\right] \\ &+ \alpha^2\mathcal{L}\left[\sqrt{\frac{N_-^e}{N_+^e}}|\ominus_-^e\rangle_n\langle\ominus_+^e| + \sqrt{\frac{N_+^e}{N_-^e}}|\ominus_+^e\rangle_n\langle\ominus_-^e|\right], \quad (43)\end{aligned}$$

where $|\ominus_\pm^e\rangle_n = N_\pm^e[D_n(\alpha) \mp D_n(-\alpha)]|1\rangle_n$, $D_n(\pm\alpha)$ are the displacement operators of the cavity mode C_n, $N_\pm^e$ are the normalization coefficients, $|\ominus_\pm^e\rangle_n$ are the first excited eigenstates of the Hamiltonian H_0, and $|1\rangle_n$ is the single-photo state of the cavity mode C_n. Here, the higher excited eigenstates of the Hamiltonian H_0 are omitted because they are almost not populated in the case of $E_{\rm gap} \gg |g_n\alpha|$ [59,63,67]. According to the terms in the second line in Eq. (43), the single-photon loss can transfer the first excited eigenstates $|\ominus_\pm^e\rangle_n$ to the ground eigenstates $|\mathcal{C}_\pm\rangle_n$. If the cavity mode C_n is initially in the cat-state subspace, it will still remain in this cat-state subspace in the presence of single-photon loss. Therefore, we can neglect the terms in the last two lines in Eq. (43) and obtain ($|\alpha| \gg 1$)

$$\mathcal{L}[a_n] \simeq \frac{\alpha^2}{\sqrt{1-e^{-4\alpha^2}}}\mathcal{L}\left[\sigma_n^x + ie^{-2\alpha^2}\sigma_n^y\right], \quad (44)$$

where $\sigma_n^x = |\mathcal{C}_+\rangle_n\langle\mathcal{C}_-| + |\mathcal{C}_-\rangle_n\langle\mathcal{C}_+|$ and $\sigma_n^y = i(|\mathcal{C}_-\rangle_n\langle\mathcal{C}_+| - |\mathcal{C}_+\rangle_n\langle\mathcal{C}_-|)$. According to Eqs. (43) and (44) and $|\alpha| \gg 1$, we can see that the single-photon loss of the cavities primarily leads to a bit-flip error σ_n^x, which is accompanied by an exponentially small phase-flip error σ_n^y. Therefore, the evolution of the cavity states will be confined in the cat-state subspace even if the system has single-photon loss.

V. CONCLUSION

In conclusion, we proposed a one-step protocol for parity measurement of N cat-state qubits. The physical model consists of N Kerr-nonlinear cavities and a superconducting qutrit. Due to the strong Kerr nonlinearity, each cavity mode evolves in a subspace spanned by the odd and even cat states, thus forming a cat-state qubit. The N Kerr-nonlinear cavities are resonantly coupled to the transition between the two higher-energy levels of the qutrit. Meanwhile, two classical fields were applied to drive the transition between the two lower-energy levels and that between the highest-energy level and the ground level of the qutrit. Modulating the classical fields with proper frequencies, we obtain an effective Hamiltonian for the parity-selective qutrit transition. According to the derived effective Hamiltonian, the qutrit can be excited to a dressed state of the two higher-energy levels after certain operations when N cat-state qubits are in even-parity states. However, when the cat-state qubits are in odd-parity states, the qutrit cannot be excited, thus remaining in the ground level. As a result, the parity of the cat-state qubits can be determined by measuring the final population of the ground level of the qutrit.

Because the systematic errors of the coupling strengths cause frequency mismatch in the effective Hamiltonian, it will decrease the accuracy of the parity measurement. In order to enhance the robustness against the systematic errors of the coupling strengths, the reverse engineering and optimal control are used to design control fields. Using the designed control fields, the parity measurement can be implemented with robustness against the systematic errors of the coupling strengths. In addition, we estimate the performance of the protocol in the presence of several disturbing factors via numerical simulations. The numerical results indicate that the protocol is also insensitive to the systematic errors of the classical fields, the inhomogeneity of the coupling strengths, the intercavity cross talk, the unwanted transitions, and decoherence. Therefore, the protocol may provide useful perspectives for the parity measurement of many cat-state qubits.

ACKNOWLEDGMENTS

Y.X. was supported by the National Natural Science Foundation of China under Grants No. 11575045 and No. 11874114, the Natural Science Funds for Distinguished Young Scholar of Fujian Province under Grant No. 2020J06011, and a project from Fuzhou University under Grant No. JG2020001-2. Y.-H.C. was supported by the National Natural Science Foundation of China under Grant No. 12304390. Y.W. was supported by the National Natural Science Foundation of China under Grant No. U21A20436.

[1] C. Bonato, F. Haupt, S. S. R. Oemrawsingh, J. Gudat, D. Ding, M. P. van Exter, and D. Bouwmeester, Phys. Rev. Lett. **104**, 160503 (2010).
[2] C. W. J. Beenakker, D. P. DiVincenzo, C. Emary, and M. Kindermann, Phys. Rev. Lett. **93**, 020501 (2004).
[3] O. P. Saira, J. P. Groen, J. Cramer, M. Meretska, G. de Lange, and L. DiCarlo, Phys. Rev. Lett. **112**, 070502 (2014).
[4] F. G. Deng, G. L. Long, and X. S. Liu, Phys. Rev. A **68**, 042317 (2003).
[5] X. S. Liu, G. L. Long, D. M. Tong, and L. Feng, Phys. Rev. A **65**, 022304 (2002).
[6] C. Meyer zu Rheda, G. Haack, and A. Romito, Phys. Rev. B **90**, 155438 (2014).
[7] B. Hage, A. Samblowski, J. DiGuglielmo, J. Fiurášek, and R. Schnabel, Phys. Rev. Lett. **105**, 230502 (2010).
[8] J. Fiurášek, Phys. Rev. A **82**, 042331 (2010).
[9] B. C. Ren, F. F. Du, and F. G. Deng, Phys. Rev. A **90**, 052309 (2014).
[10] Y. B. Sheng, L. Zhou, and G. L. Long, Phys. Rev. A **88**, 022302 (2013).
[11] P. S. Yan, L. Zhou, W. Zhong, and Y. B. Sheng, Sci. China: Phys., Mech. Astron. **66**, 250301 (2023).
[12] J. W. Pan, D. Bouwmeester, H. Weinfurter, and A. Zeilinger, Phys. Rev. Lett. **80**, 3891 (1998).
[13] M. Halder, A. Beveratos, N. Gisin, V. Scarani, C. Simon, and H. Zbinden, Nat. Phys. **3**, 692 (2007).
[14] W. Ning, X. J. Huang, P. R. Han, H. Li, H. Deng, Z. B. Yang, Z. R. Zhong, Y. Xia, K. Xu, D. Zheng, and S. B. Zheng, Phys. Rev. Lett. **123**, 060502 (2019).
[15] F. Ozaydin, S. Bugu, C. Yesilyurt, A. A. Altintas, M. Tame, and Ş. K. Özdemir, Phys. Rev. A **89**, 042311 (2014).
[16] X. P. Zang, M. Yang, W. Song, and Z. L. Cao, Opt. Commun. **370**, 168 (2016).
[17] Y. Q. Ji, X. Q. Shao, and X. X. Yi, Sci. Rep. **7**, 1378 (2017).
[18] C. H. Bennett, G. Brassard, C. Crépeau, R. Jozsa, A. Peres, and W. K. Wootters, Phys. Rev. Lett. **70**, 1895 (1993).
[19] A. Karlsson and M. Bourennane, Phys. Rev. A **58**, 4394 (1998).
[20] J. W. Pan, M. Daniell, S. Gasparoni, G. Weihs, and A. Zeilinger, Phys. Rev. Lett. **86**, 4435 (2001).
[21] L. Sun, A. Petrenko, Z. Leghtas, B. Vlastakis, G. Kirchmair, K. M. Sliwa, A. Narla, M. Hatridge, S. Shankar, J. Blumoff, L. Frunzio, M. Mirrahimi, M. H. Devoret, and R. J. Schoelkopf, Nature (London) **511**, 444 (2014).
[22] K. Nemoto and W. J. Munro, Phys. Rev. Lett. **93**, 250502 (2004).
[23] Y. B. Sheng and F. G. Deng, Phys. Rev. A **81**, 032307 (2010).
[24] Y. B. Sheng, F. G. Deng, and G. L. Long, Phys. Rev. A **82**, 032318 (2010).
[25] M. Sisodia, A. Shukla, and A. Pathak, Phys. Lett. A **381**, 3860 (2017).
[26] B. Trauzettel, A. N. Jordan, C. W. J. Beenakker, and M. Büttiker, Phys. Rev. B **73**, 235331 (2006).
[27] Y. Xiao, R. H. Zheng, Y. Liu, Y. H. Kang, J. Song, and Y. Xia, Ann. Phys. (Berlin, Ger.) **534**, 2100461 (2022).
[28] Y. Xiao, Y. H. Kang, R. H. Zheng, Y. Liu, Y. Wang, J. Song, and Y. Xia, Adv. Quantum Technol. **6**, 2200192 (2023).
[29] R. H. Zheng, Y. H. Kang, Z. C. Shi, and Y. Xia, Ann. Phys. (Berlin, Ger.) **530**, 1800133 (2018).
[30] S. L. Su, F. Q. Guo, L. Tian, X. Y. Zhu, L. L. Yan, E. J. Liang, and M. Feng, Phys. Rev. A **101**, 012347 (2020).
[31] R. H. Zheng, Y. H. Kang, S. L. Su, J. Song, and Y. Xia, Phys. Rev. A **102**, 012609 (2020).
[32] Y. Ning, Y. H. Kang, Z. C. Shi, J. Song, and Y. Xia, Laser Phys. Lett. **17**, 125204 (2020).
[33] J. R. Samal, M. Gupta, P. K. Panigrahi, and A. Kumar, J. Phys. B **43**, 095508 (2010).
[34] S. B. van Dam, J. Cramer, T. H. Taminiau, and R. Hanson, Phys. Rev. Lett. **123**, 050401 (2019).
[35] L. Hu, Y. Ma, W. Cai, X. Mu, Y. Xu, W. Wang, Y. Wu, H. Wang, Y. P. Song, C. L. Zou, S. M. Girvin, L. M. Duan, and L. Sun, Nat. Phys. **15**, 503 (2019).
[36] Z. D. Walton, A. F. Abouraddy, A. V. Sergienko, B. E. A. Saleh, and M. C. Teich, Phys. Rev. Lett. **91**, 087901 (2003).
[37] E. Kapit, Phys. Rev. Lett. **120**, 050503 (2018).
[38] B. Shaw, M. M. Wilde, O. Oreshkov, I. Kremsky, and D. A. Lidar, Phys. Rev. A **78**, 012337 (2008).
[39] Y. B. Sheng and L. Zhou, Sci. Rep. **5**, 13453 (2015).
[40] Y. Ma, Y. Xu, X. Mu, W. Cai, L. Hu, W. Wang, X. Pan, H. Wang, Y. P. Song, C. L. Zou, and L. Sun, Nat. Phys. **16**, 827 (2020).
[41] J. Zhang, R. Laflamme, and D. Suter, Phys. Rev. Lett. **109**, 100503 (2012).
[42] G. F. Xu, J. Zhang, D. M. Tong, E. Sjöqvist, and L. C. Kwek, Phys. Rev. Lett. **109**, 170501 (2012).

[43] J. Zhang, S. J. Devitt, J. Q. You, and F. Nori, Phys. Rev. A **97**, 022335 (2018).

[44] M. K. Henry, C. Ramanathan, J. S. Hodges, C. A. Ryan, M. J. Ditty, R. Laflamme, and D. G. Cory, Phys. Rev. Lett. **99**, 220501 (2007).

[45] C. Wu, Y. Wang, X. L. Feng, and J. L. Chen, Phys. Rev. Appl. **13**, 014055 (2020).

[46] A. deMarti iOlius, J. E. Martinez, P. Fuentes, P. M. Crespo, and J. Garcia-Frias, Phys. Rev. A **106**, 062428 (2022).

[47] L. Zhou and Y. B. Sheng, Sci. Rep. **6**, 28813 (2016).

[48] R. W. Heeres, P. Reinhold, N. Ofek, L. Frunzio, L. Jiang, M. H. Devoret, and R. J. Schoelkopf, Nat. Commun. **8**, 94 (2017).

[49] W. Cai, Y. Ma, W. Wang, C.-L. Zou, and L. Sun, Fundam. Res. **1**, 50 (2021).

[50] M. H. Michael, M. Silveri, R. T. Brierley, V. V. Albert, J. Salmilehto, L. Jiang, and S. M. Girvin, Phys. Rev. X **6**, 031006 (2016).

[51] V. V. Albert, K. Noh, K. Duivenvoorden, D. J. Young, R. T. Brierley, P. Reinhold, C. Vuillot, L. Li, C. Shen, S. M. Girvin, B. M. Terhal, and L. Jiang, Phys. Rev. A **97**, 032346 (2018).

[52] Y. H. Kang, J. Song, and Y. Xia, Opt. Lett. **47**, 4099 (2022).

[53] J. M. Gertler, B. Baker, J. Li, S. Shirol, J. Koch, and C. Wang, Nature (London) **590**, 243 (2021).

[54] A. Denys and A. Leverrier, Quantum **7**, 1032 (2023).

[55] B. Vlastakis, G. Kirchmair, Z. Leghtas, S. E. Nigg, L. Frunzio, S. M. Girvin, M. Mirrahimi, M. H. Devoret, and R. J. Schoelkopf, Science **342**, 607 (2013).

[56] V. V. Albert, S. O. Mundhada, A. Grimm, S. Touzard, M. H. Devoret, and L. Jiang, Quantum Sci. Technol. **4**, 035007 (2019).

[57] Y. H. Chen, W. Qin, R. Stassi, X. Wang, and F. Nori, Phys. Rev. Res. **3**, 033275 (2021).

[58] V. V. Albert, C. Shu, S. Krastanov, C. Shen, R. B. Liu, Z. B. Yang, R. J. Schoelkopf, M. Mirrahimi, M. H. Devoret, and L. Jiang, Phys. Rev. Lett. **116**, 140502 (2016).

[59] M. Mirrahimi, Z. Leghtas, V. V. Albert, S. Touzard, R. J. Schoelkopf, L. Jiang, and M. H. Devoret, New J. Phys. **16**, 045014 (2014).

[60] C. Chamberland, K. Noh, P. Arrangoiz-Arriola, E. T. Campbell, C. T. Hann, J. Iverson, H. Putterman, T. C. Bohdanowicz, S. T. Flammia, A. Keller, G. Refael, J. Preskill, L. Jiang, A. H. Safavi-Naeini, O. Painter, and F. G. S. L. Brandao, PRX Quantum **3**, 010329 (2022).

[61] Y. Xu, Y. Ma, W. Cai, X. Mu, W. Dai, W. Wang, L. Hu, X. Li, J. Han, H. Wang, Y. P. Song, Z. B. Yang, S. B. Zheng, and L. Sun, Phys. Rev. Lett. **124**, 120501 (2020).

[62] Y. H. Chen, W. Qin, X. Wang, A. Miranowicz, and F. Nori, Phys. Rev. Lett. **126**, 023602 (2021).

[63] J. Guillaud and M. Mirrahimi, Phys. Rev. X **9**, 041053 (2019).

[64] N. Ofek, A. Petrenko, R. Heeres, P. Reinhold, Z. Leghtas, B. Vlastakis, Y. Liu, L. Frunzio, S. M. Girvin, L. Jiang, M. Mirrahimi, M. H. Devoret, and R. J. Schoelkopf, Nature (London) **536**, 441 (2016).

[65] Y. Zhang, X. Zhao, Z. F. Zheng, L. Yu, Q. P. Su, and C. P. Yang, Phys. Rev. A **96**, 052317 (2017).

[66] T. Kanao, S. Masuda, S. Kawabata, and H. Goto, Phys. Rev. Appl. **18**, 014019 (2022).

[67] Y. H. Chen, R. Stassi, W. Qin, A. Miranowicz, and F. Nori, Phys. Rev. Appl. **18**, 024076 (2022).

[68] Y. H. Kang, Y. H. Chen, X. Wang, J. Song, Y. Xia, A. Miranowicz, S. B. Zheng, and F. Nori, Phys. Rev. Res. **4**, 013233 (2022).

[69] Q. P. Su, Y. Zhang, and C. P. Yang, Phys. Rev. A **105**, 062436 (2022).

[70] Y. H. Kang, Y. Xiao, Z. C. Shi, Y. Wang, J. Q. Yang, J. Song, and Y. Xia, New J. Phys. **25**, 033029 (2023).

[71] A. Grimm, N. E. Frattini, S. Puri, S. O. Mundhada, S. Touzard, M. Mirrahimi, S. M. Girvin, S. Shankar, and M. H. Devoret, Nature (London) **584**, 205 (2020).

[72] S. Puri, S. Boutin, and A. Blais, npj Quantum Inf. **3**, 18 (2017).

[73] X. Chen and J. G. Muga, Phys. Rev. A **86**, 033405 (2012).

[74] Y. H. Kang, Z. C. Shi, B. H. Huang, J. Song, and Y. Xia, Phys. Rev. A **101**, 032322 (2020).

[75] A. Ruschhaupt, X. Chen, D. Alonso, and J. G. Muga, New J. Phys. **14**, 093040 (2012).

[76] X. T. Yu, Q. Zhang, Y. Ban, and X. Chen, Phys. Rev. A **97**, 062317 (2018).

[77] X. Chen, E. Torrontegui, and J. G. Muga, Phys. Rev. A **83**, 062116 (2011).

[78] Y. Z. Lai, J. Q. Liang, H. J. W. Müller-Kirsten, and J. G. Zhou, Phys. Rev. A **53**, 3691 (1996).

[79] E. S. Kyoseva and N. V. Vitanov, Phys. Rev. A **73**, 023420 (2006).

[80] P. A. Ivanov, E. S. Kyoseva, and N. V. Vitanov, Phys. Rev. A **74**, 022323 (2006).

[81] B. Rousseaux, S. Guérin, and N. V. Vitanov, Phys. Rev. A **87**, 032328 (2013).

[82] B. H. Huang, Y. H. Kang, Y. H. Chen, Q. C. Wu, J. Song, and Y. Xia, Phys. Rev. A **96**, 022314 (2017).

[83] H. R. Lewis and W. B. Riesenfeld, J. Math. Phys. **10**, 1458 (1969).

[84] L. Van-Damme, D. Schraft, G. T. Genov, D. Sugny, T. Halfmann, and S. Guérin, Phys. Rev. A **96**, 022309 (2017).

[85] D. Daems, A. Ruschhaupt, D. Sugny, and S. Guérin, Phys. Rev. Lett. **111**, 050404 (2013).

[86] X. J. Lu, X. Chen, A. Ruschhaupt, D. Alonso, S. Guérin, and J. G. Muga, Phys. Rev. A **88**, 033406 (2013).

[87] C. P. Yang, Q. P. Su, S. B. Zheng, and F. Nori, Phys. Rev. A **93**, 042307 (2016).

[88] K. Inomata, T. Yamamoto, P. M. Billangeon, Y. Nakamura, and J. S. Tsai, Phys. Rev. B **86**, 140508(R) (2012).

[89] S. Liu, Y. H. Chen, Y. Wang, Y. H. Kang, Z. C. Shi, J. Song, and Y. Xia, Phys. Rev. A **106**, 042430 (2022).

[90] A. O. Niskanen, K. Harrabi, F. Yoshihara, Y. Nakamura, S. Lloyd, and J. S. Tsai, Science **316**, 723 (2007).

[91] Z. H. Peng, Y. X. Liu, J. T. Peltonen, T. Yamamoto, J. S. Tsai, and O. Astafiev, Phys. Rev. Lett. **115**, 223603 (2015).

[92] T. Liu, Y. H. Zhou, Q. C. Wu, and C. P. Yang, Appl. Phys. Lett. **121**, 244001 (2022).

[93] C. Rigetti, J. M. Gambetta, S. Poletto, B. L. T. Plourde, J. M. Chow, A. D. Córcoles, J. A. Smolin, S. T. Merkel, J. R. Rozen, G. A. Keefe, M. B. Rothwell, M. B. Ketchen, and M. Steffen, Phys. Rev. B **86**, 100506(R) (2012).

[94] F. Yan, S. Gustavsson, A. Kamal, J. Birenbaum, A. P. Sears, D. Hover, T. J. Gudmundsen, D. Rosenberg, G. Samach, S. Weber, J. L. Yoder, T. P. Orlando, J. Clarke, A. J. Kerman, and W. D. Oliver, Nat. Commun. **7**, 12964 (2016).

[95] J. Q. You, X. Hu, S. Ashhab, and F. Nori, Phys. Rev. B **75**, 140515(R) (2007).